

Polarization control of above-threshold ionization spectrum in elliptically polarized two-color laser fields

Fa-Cheng Jin(金发成), Hui-Hui Yang(杨慧慧), Xiao-Hong Song(宋晓红), Fei Li(李飞), Ling-Ling Du(杜玲玲), Hong-Jie Xue(薛红杰), Li-Min Wei(魏丽敏), Yue Bai(白悦), Hao-Xiang Liu(刘浩翔), Bing-Bing Wang(王兵兵), and Wei-Feng Yang(杨玮枫)

Citation: Chin. Phys. B, 2024, 33 (**4**): 043301. DOI: 10.1088/1674-1056/ad24d8
Journal homepage: http://cpb.iphy.ac.cn; http://iopscience.iop.org/cpb

What follows is a list of articles you may be interested in

Revising the $H_2{}^{16}O$ line-shape parameters around 1.1 μm based on the speed-dependent Nelkin-Ghatak profile and the Hartmann-Tran profile

Hui Zhang(张惠), Jianjie Zheng(郑健捷), Qiang Liu(刘强), Wenyue Zhu(朱文越), Xianmei Qian(钱仙妹), Guisheng Jiang(江贵生), Shenlong Zha(查申龙), Qilei Zhang(张启磊), and Hongliang Ma(马宏亮)
Chin. Phys. B, 2023, 32 (**12**): 123301. DOI: 10.1088/1674-1056/acc7f5

Elliptically polarized high-order harmonic generation in nitrogen molecules with cross-linearly polarized two-color laser fields

Chunyang Zhai(翟春洋), Yinmeng Wu(吴银梦), Lingling Qin(秦玲玲), Xiang Li(李翔), Luke Shi(史璐珂), Ke Zhang(张可), Shuaijie Kang(康帅杰), Zhengfa Li(李整法), Yingbin Li(李盈傧), Qingbin Tang(汤清彬), and Benhai Yu(余本海)
Chin. Phys. B, 2023, 32 (**7**): 073301. DOI: 10.1088/1674-1056/acad70

Hydrogen sulphide detection using near-infrared diode laser and compact dense-pattern multipass cell

Xing Tian(田兴), Yuan Cao(曹渊), Jia-Jin Chen(陈家金), Kun Liu(刘锟), Gui-Shi Wang(王贵师), Xiao-Ming Gao(高晓明)
Chin. Phys. B, 2019, 28 (**6**): 063301. DOI: 10.1088/1674-1056/28/6/063301

Influence factor analysis of field-free molecular orientation

Jing-Song Liu(刘劲松), Qi-Yuan Cheng(程起元), Da-Guang Yue(岳大光), Xu-Cong Zhou(周旭聪), Qing-Tian Meng(孟庆田)
Chin. Phys. B, 2018, 27 (**3**): 033301. DOI: 10.1088/1674-1056/27/3/033301

Low-energy structure in the ionization of argon: Comparison of experiment with theory

Feng Li-Qiang (冯立强), Chu Tian-Shu (楚天舒), Wang Li (王利)
Chin. Phys. B, 2013, 22 (**2**): 023302. DOI: 10.1088/1674-1056/22/2/023302

RAPID COMMUNICATION

Polarization control of above-threshold ionization spectrum in elliptically polarized two-color laser fields

Fa-Cheng Jin(金发成)[1,5,†], Hui-Hui Yang(杨慧慧)[1], Xiao-Hong Song(宋晓红)[2,3], Fei Li(李飞)[5], Ling-Ling Du(杜玲玲)[5], Hong-Jie Xue(薛红杰)[1], Li-Min Wei(魏丽敏)[1], Yue Bai(白悦)[1], Hao-Xiang Liu(刘浩翔)[1], Bing-Bing Wang(王兵兵)[4,6,‡], and Wei-Feng Yang(杨玮枫)[2,3,§]

[1] *Faculty of Science, Xi'an Aeronautical Institute, Xi'an* 710077, *China*
[2] *School of Physics and Optoelectronic Engineering, Hainan University, Haikou* 570288, *China*
[3] *Center for Theoretical Physics, Hainan University, Haikou* 570288, *China*
[4] *Laboratory of Optical Physics, Beijing National Laboratory for Condensed Matter Physics, Institute of Physics, Chinese Academy of Sciences, Beijing* 100190, *China*
[5] *College of Science, Shantou University, Shantou* 515063, *China*
[6] *University of Chinese Academy of Sciences, Beijing* 100049, *China*

(Received 24 December 2023; revised manuscript received 19 January 2024; accepted manuscript online 1 February 2024)

We study the above-threshold ionization (ATI) process of atoms exposed to fundamental and high-frequency lasers with arbitrary ellipticity by applying the frequency-domain theory. It is found that the angular-resolved ATI spectrum is sensitive to ellipticities of two lasers and emitted angles of the photoelectron. Particularly for the photon energy of the high-frequency laser more than atomic ionization potential, the width of plateau tends to a constant with increasing ellipticity of fundamental field, the dip structure disappears with increasing ellipticity of the high-frequency field. With the help of the quantum channel analysis, it is shown that the angular distribution depends mainly on the ellipticity of high-frequency field in the case that its frequency is high. Moreover, one can see that the maximal and minimal energies in quantum numerical results are in good agreement with the classical prediction. Our investigation may provide theoretical support for experimental research on polarization control of ionization in elliptically polarized two-color laser fields.

Keywords: above-threshold ionization, two-color laser, polarization control

PACS: 33.20.Ea, 33.20.Ni, 33.20.Xx, 33.60.+q **DOI:** 10.1088/1674-1056/ad24d8

1. Introduction

When an atomic or molecular system is exposed to an intense laser, it may absorb more laser-field photons than the minimum number required for ionization, which is called above-threshold ionization (ATI). This process as one of the most fundamental strong-field phenomena has attracted considerable attention in both experimental and theoretical studies (for some reviews, see, e.g., Refs. [1,2]) since its first observation by Agostini *et al*.[3] Because of their great contribution to attosecond science, P. Agostini won the Nobel Prize in Physics in 2023. The ATI is governed by the laser field and Coulomb potential, thus the photoelectron spectrum can be in favor to extract either information about the laser field itself,[4–7] or about the structure of the target.[8–10]

Over the past decade, it has been proved that the ATI process can be controlled by a tailored laser.[9,11] In contrast to the case of a monochromatic field, two-color laser field has been extensively used to offer significant additional degrees of freedom for manipulation in ionization process. Generally, a phase-controlled two-color laser pulse was used to control the transition dynamic of target.[12–14] The manipulation of the wave packets could be achieved by the orthogonally polarized two-color laser fields.[15,16] Compared with linearly polarized laser fields, elliptically polarized laser fields provided more dimensions for altering and further controling the motion of electron wave packets in ionization process.[17,18] The bicircular ATI from atom or molecule was explored.[19–21] Electron-ion radiative recombination assisted by a bichromatic elliptically polarized laser field was investigated.[22]

It is well-known that the high-order harmonic generation or free-electron laser radiation provides an ideal light source for producing extreme ultraviolet (XUV) laser.[23–25] It has been proved that the ionization channel of atom via two-photon absorption can be effectively controlled by the elliptically polarized XUV lasers[26] and biharmonic ($\omega + 2\omega$) fields.[27] These results may show the feasibility of polarization control on ionization process by laser ellipticity. It is noticed that XUV laser, together with an additional infrared (IR) laser, allows ionization of atoms or molecules. The polarization state of the two lasers can always be achieved by controlling from linear to elliptical polarization.[28–30] The photoelectron spectrum of atom in the IR+XUV fields with the same

[†]Corresponding author. E-mail: fchjin@163.com
[‡]Corresponding author. E-mail: wbb@aphy.iphy.ac.cn
[§]Corresponding author. E-mail: wfyang@hainanu.edu.cn

© 2024 Chinese Physical Society and IOP Publishing Ltd

linearly polarized directions shows a sideband,[30] which can decouple rich information of target and laser.[31,32] Further, it is reported that the angular distribution obviously depends on polarization directions of IR and XUV lasers in the experimental aspect.[33,34]

To the best of our knowledge, it is noticed that the above ionization phenomenon occurs almost in the interaction of atom or molecule with the linearly polarized two-color lasers, while the ATI process under IR+XUV fields with arbitrary ellipticity is comparatively less studied. In this paper, we will discuss the ATI process in elliptically polarized fundamental and high-frequency lasers, by applying the frequency-domain theory based on the nonperturbative quantum electrodynamics theoretical approach.[35] The frequency-domain theory was developed to study the ATI in 1989,[36] and then was extended to discuss the high-harmonic generation,[37] high-order ATI[38,39] and nonsequential double ionization[40–42] processes. Further, the relationship between the time-domain and frequency-domain theories in strong-field physics was demonstrated.[43] Recently, we used this theory to study the angular-resolved ATI spectrum in the orthogonally polarized IR+XUV lasers, and the ATI spectrum shows the dip structure in different plateau, which is attributed to the relation of absorbing XUV photons and polarization direction of XUV laser.[44] It was demonstrated that the ATI spectrum can be effectively controlled by changing polarization directions of linearly polarized lasers.[45] In this work, we first show the effects of the ellipticities of the two lasers on angular-resolved ATI spectrum. Then with the help of the channel analysis, multiplateau formation is revealed. Finally, the saddle-point approximation is used, the energy orbit in the elliptically polarized two-color lasers is obtained and well predicts the width of each plateau. This result indicates the ATI process can be effectively controlled by ellipticity of lasers.

This paper is organized as follows. We give an overview of the theoretical method in Section 2. Next we discuss the influence of the elliptically polarized fundamental and high-frequency lasers on angular-resolved ATI spectrum in Section 3. Finally, in Section 4, a summary of this work is provided. Atomic units are used throughout unless otherwise stated.

2. Theoretical method

The frequency-domain theory of ATI process for atoms illuminated by a two-color laser has been explored,[35,46,47] where the strong-field approximation[48,49] is used. The interaction of atoms and lasers can be viewed as an isolated system, thus the energy conservation of this system is satisfied during the total transition process. The transition matrix of the whole system from the initial state $\psi_{\rm i}$ to the final state $\psi_{\rm f}$ can be written as[35,39]

$$T_{\rm fi} = \langle\psi_{\rm f}|V|\psi_{\rm i}\rangle + \langle\psi_{\rm f}|U\frac{1}{E_{\rm i}-H+{\rm i}\varepsilon}V|\psi_{\rm i}\rangle. \tag{1}$$

In the above, the first and second terms represent the direct and rescattering ATI processes, respectively. Therefore, the transition matrix can be expressed as $T_{\rm fi} = T_{\rm d} + T_{\rm r}$, where $T_{\rm d}$ represents the direct transition of the electron from the initial state to the final state, and $T_{\rm r}$ represents the rescattering process where the electron recollides with the core after it is ionized by the laser field from the initial state. The Hamiltonian $H = H_0 + U(\boldsymbol{r}) + V$ with the free-electron and free-photon operator H_0, the atomic binding potential $U(\boldsymbol{r})$ and the electron–photon interaction $V = -\sum_{t=1,2}[(-{\rm i}\nabla)\cdot\boldsymbol{A}_t(-\boldsymbol{k}_t\cdot\boldsymbol{r}) + \boldsymbol{A}_t(-\boldsymbol{k}_t\cdot\boldsymbol{r})\cdot(-{\rm i}\nabla)]/2 + [\sum_{t=1,2}\boldsymbol{A}_t(-\boldsymbol{k}_t\cdot\boldsymbol{r})]^2/2$. Here the vector potential is given by $\boldsymbol{A}_t(-\boldsymbol{k}_t\cdot\boldsymbol{r}) = (2V_{{\rm e}_t}\omega_t)^{-1/2}(\widehat{\varepsilon}_t\,{\rm e}^{\boldsymbol{k}_t\cdot\boldsymbol{r}}a_t + \widehat{\varepsilon}_t^*\,{\rm e}^{-\boldsymbol{k}_t\cdot\boldsymbol{r}}a_t^\dagger)$, where $\boldsymbol{k}_t$ is the wave vector, $V_{{\rm e}_t}$ is the normalization volume of the photon field, and ω_t is laser frequency for $t = 1$ or 2. The polarization vector of the laser field is expressed by $\hat{\varepsilon}_t = \hat{x}\cos(\xi_t/2) + {\rm i}\hat{y}\sin(\xi_t/2)$. The ellipticity is defined as $\eta_t = \tan(\xi_t/2)$, which monitors the degree of polarization, such that $\eta_t = 0$ corresponds to linear polarization, $\eta_t = 1.0$ corresponds to circular polarization, and the open interval $(0, 1.0)$ corresponds to the elliptical polarization. In Eq. (1) the initial state of the system can be expressed by $|\psi_{\rm i}\rangle = \phi_{\rm i}(\boldsymbol{r})\otimes|n_1\rangle\otimes|n_2\rangle$ with the energy $E_{\rm i} = -I_{\rm p} + \sum_{t=1,2}(n_t + 1/2)\omega_t$, $\phi_{\rm i}(\boldsymbol{r})$ is the ground-state wavefunction of the atom, $I_{\rm p}$ is the ionization threshold, and $|n_t\rangle$ is the Fock state of the laser with the photon number n_t. The final state $|\psi_{\rm f}\rangle = |\psi_{\boldsymbol{p}_{\rm f},m_1m_2}(\boldsymbol{r})\rangle$ is the quantized-field Volkov state in the two-color laser field[35]

$$\begin{aligned}|\Psi_{\boldsymbol{p}_{\rm f},m_1m_2}(\boldsymbol{r})\rangle = V_{\rm e}^{-1/2}\sum_{\substack{j_1=-m_1\\ j_2=-m_2}}^{\infty}\exp\Big\{{\rm i}\Big[\boldsymbol{p}_{\rm f} + (u_{{\rm p}_1}-j_1)\boldsymbol{k}_1 \\ +(u_{{\rm p}_2}-j_2)\boldsymbol{k}_2\Big]\cdot\boldsymbol{r}\Big\} \\ \times\mathcal{X}_{j_1j_2}(z_{\rm f})^*|m_1+j_1, m_2+j_2\rangle,\end{aligned} \tag{2}$$

with the energy $E_{\rm f} = \boldsymbol{p}_{\rm f}^2/2 + \sum_{t=1,2}\left[(n_t+1/2)\omega_t + u_{{\rm p}_t}\omega_t\right]$. Here $\boldsymbol{p}_{\rm f}$ is the final momentum of the ionized electron, and $u_{{\rm p}_t}$ is calculated by the ponderomotive energy $U_{{\rm p}_t}$ in units of frequency ω_t. m_t is the number of background photons. The generalized phased Bessel function $\mathcal{X}_{j_1j_2}(z_{\rm f})$ in Eq. (2) is expressed by[35]

$$\begin{aligned}\mathcal{X}_{j_1j_2}(z_{\rm f}) = \sum_{j_3j_4j_5j_6}X_{-j_1+2j_3+j_5+j_6}(z_1)X_{-j_2+2j_4+j_5-j_6}(z_2) \\ \times X_{-j_3}(z_3)X_{-j_4}(z_4)X_{-j_5}(z_5)X_{-j_6}(z_6),\end{aligned} \tag{3}$$

where six arguments are always complex and defined as $z_1 = 2\sqrt{u_{{\rm p}_1}/\omega_1}\boldsymbol{p}_{\rm f}\cdot\widehat{\epsilon}_1$, $z_2 = 2\sqrt{u_{{\rm p}_2}/\omega_2}\boldsymbol{p}_{\rm f}\cdot\widehat{\epsilon}_2$, $z_3 = u_{{\rm p}_1}/2\widehat{\epsilon}_1\cdot\widehat{\epsilon}_1$, $z_4 = u_{{\rm p}_2}/2\widehat{\epsilon}_2\cdot\widehat{\epsilon}_2$, $z_5 = 2\sqrt{u_{{\rm p}_1}\omega_1u_{{\rm p}_2}\omega_2}/(\omega_1+\omega_2)\widehat{\epsilon}_1\cdot\widehat{\epsilon}_2$, and $z_6 = 2\sqrt{u_{{\rm p}_1}\omega_1u_{{\rm p}_2}\omega_2}/|\omega_1-\omega_2|\widehat{\epsilon}_1\cdot\widehat{\epsilon}_2^*$. The phased Bessel function $X_m(z)$ has been discussed[50] and is given by $X_m(z) = J_m(|z|)\,{\rm e}^{{\rm i}m\vartheta}$ with $z = |z|\,{\rm e}^{{\rm i}\vartheta}$, $J_m(|z|)$ is the ordinary Bessel function of order m.

In this work, it is assumed that the fundamental field with frequency ω_1 is the IR laser and the second one with frequency

ω_2 is the high-frequency laser. Since ω_2 is much larger than ω_1, the contribution of the rescattering process in Eq. (1) to ATI process is much smaller than that of the direct process under the condition of our present computational parameters, thus we only consider the direct ATI process in the following. Using the initial and final states in Eq. (2), the first term in Eq. (1) can be rewritten as[35,47]

$$\boldsymbol{T}_{\rm d} = V_{\rm e}^{-1/2}[(u_{\rm p_1} - s_1)\omega_1 + (u_{\rm p_2} - s_2)\omega_2]\mathcal{X}_{s_1 s_2}(Z_{\rm f})\Phi(\boldsymbol{p}_{\rm f}), \quad (4)$$

where s_1 and s_2 are the photon numbers absorbed from the two laser fields with frequencies ω_1 and ω_2, respectively. In the above, $\Phi(\boldsymbol{p}_{\rm f})$ is Fourier transformation of $\phi_{\rm i}(\boldsymbol{r})$, and can be expressed by $\Phi(\boldsymbol{p}_{\rm f}) = (4\pi/\alpha)^{3/4}\exp[-(\boldsymbol{p}_{\rm f}^2/2\alpha)]$ with $\alpha = 2I_{\rm p}$.[43] The ionization rate is given by[35]

$$\frac{{\rm d}W}{{\rm d}\Omega} = \frac{V_{\rm e}}{(2\pi)^2}\int_0^\infty \boldsymbol{p}_{\rm f}^2\,{\rm d}|\boldsymbol{p}_{\rm f}||T_{\rm d}|^2 2\pi\delta\left(E_{\rm f} - E_{\rm i}\right), \quad (5)$$

where ${\rm d}\Omega_{\boldsymbol{p}_{\rm f}} = \sin\theta_{\rm f}{\rm d}\theta_{\rm f}{\rm d}\varphi_{\rm f}$ is the differential solid angle of the ionized electron with the momentum $\boldsymbol{p}_{\rm f}$, $\theta_{\rm f}$ and $\varphi_{\rm f}$ are its polar and azimuthal angles. In this theory, a Fock state is taken as the state of the laser field. Although a coherent state is more appropriate for describing the laser field, it will not affect our results.[43]

3. Results and discussion

In this section, we only consider the direct ATI process of hydrogen atoms in elliptically polarized fundamental and high-frequency lasers, where the polarization direction is in the *xoy* plane, as shown in Fig. 1. The ionization probability is only considered in the polarization plane, and the ionization along the z-axis is neglected. Here the fundamental field is IR laser with wavelength $\lambda_1 = 1064$ nm corresponding to the frequency $\omega_1 = 1.16$ eV, the intensities of both two lasers are $I_1 = I_2 = 1.0\times10^{12}$ W/cm^2. Under the present parameters of lasers, the ionization probability of rescattering process is much lower than that of direct ionization, hence the contribution of rescattering process to total ionization can be negligible. The emitted angle of photoelectron is defined by the azimuthal direction $\varphi_{\rm f}$ between the emission direction of the ionized electron and the x axis in the following text.

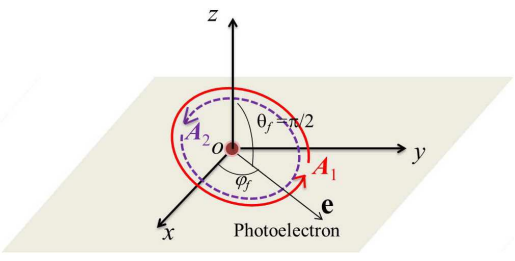


Fig. 1. Coordinate system of hydrogen atom upon photoelectron emission. The solid (red) and dash (violet) lines represent the vector potentials of fundamental and high-frequency lasers, where their polarization directions are in the *xoy* plane, i.e., $\theta_{\rm f} = \pi/2$, and $\varphi_{\rm f}$ represents the angle between the emission direction of the photoelectron and the x axis.

3.1. ATI spectrum and channel analysis

We now consider the influence of the ellipticity of the fundamental laser on the ATI process. Figure 2 shows the angular-resolved ATI spectra for $\omega_2 = 3\omega_1$ ((a1)–(d1)), $7\omega_1$ ((a2)–(d2)), $15\omega_1$ ((a3)–(d3)), $25\omega_1$ ((a4)–(d4)) and for ellipticities $\eta_1 = 0$ ((a1)–(a4)), 0.27 ((b1)–(b4)), 0.58 ((c1)–(c4)) and 1.0 ((d1)–(d4)), where $\eta_2 = 0$. In Fig. 2(a1), the ionized electron is mainly distributed in the lower-energy regions, and the photoelectron energy is larger and its distribution is wider when electron is emitted along the x axis (i.e., $\varphi_{\rm f} = 0^\circ$ or 180°) than other emitted angles, while the ionization probabilities around $\varphi_{\rm f} = 60^\circ$ or 120° are higher. From Figs. 2(a1)–2(d1), one can see that the distributions of the photoelectron energy change as the increase of ellipticity η_1. Especially for the IR laser being circularly polarized $\eta_1 = 1.0$, the ionization probabilities around $\varphi_{\rm f} = 90^\circ$ increase. As shown in Figs. 2(a2)–2(d2), for $\omega_2 = 7\omega_1$, the angular-resolved ATI spectrum shows the higher- and lower-energy parts, where the probabilities of the lower-energy parts are much higher than that of the higher-energy parts, and the distributions of angular-resolved ATI spectra change with increasing η_1. It is further found that the number of the dip structures in the higher-energy parts is more than that in the lower-energy parts. As shown in Figs. 2(a3)–2(d3) and 2(a4)–2(d4), where the photon energies of the high-frequency lasers are much higher than the ionization potential, there are two plateaus in the angular-resolved ATI spectra for any η_1, where the ionization probability of the first plateau is much larger than that of the second plateau. It is also seen that the dip structures in each plateau appear, where there are two dip structures in the second plateau and one structure in the first plateau. The dip structure for $\varphi_{\rm f} = 0$ is attributed to the fact that the electron cannot absorb one XUV photon when its emission direction is perpendicular to the XUV laser polarization, and other dip structures are caused by the coherent results of different channels.[44,45] The energy width of each plateau, defined as the difference between the maximum and minimum energies of corresponding plateau, is sensitive to the emitted angle $\varphi_{\rm f}$ when $\eta_1 < 1.0$. Moreover, no matter what the emitted angle $\varphi_{\rm f}$ is, the energy width of each plateau tends to be the same with the increase of η_1, and the difference of the ionization probabilities of two adjacent plateaus increases with ω_2. The above results indicate that the ATI spectrum is sensitive to the ellipticity η_1 of the fundamental field and emitted angle.

To consider the effect of the ellipticity of the high-frequency laser on ionization process, Fig. 3 shows the angular-resolved ATI spectra for $\omega_2 = 3\omega_1$ ((a1)–(c1)), $7\omega_1$ ((a2)–(c2)), $15\omega_1$ ((a3)–(c3)), $25\omega_1$ ((a4)–(c4)) and for $\eta_2 = 0.27$ ((a1)–(a4)), 0.58 ((b1)–(b4)), 1.0 ((c1)–(c4)), where IR laser is linearly polarized, i.e., $\eta_1 = 0$. From Figs. 3(a1) to 3(c1), one can see that distributions of the angular-resolved ATI spectra also depend on the ellipticity η_2, and the

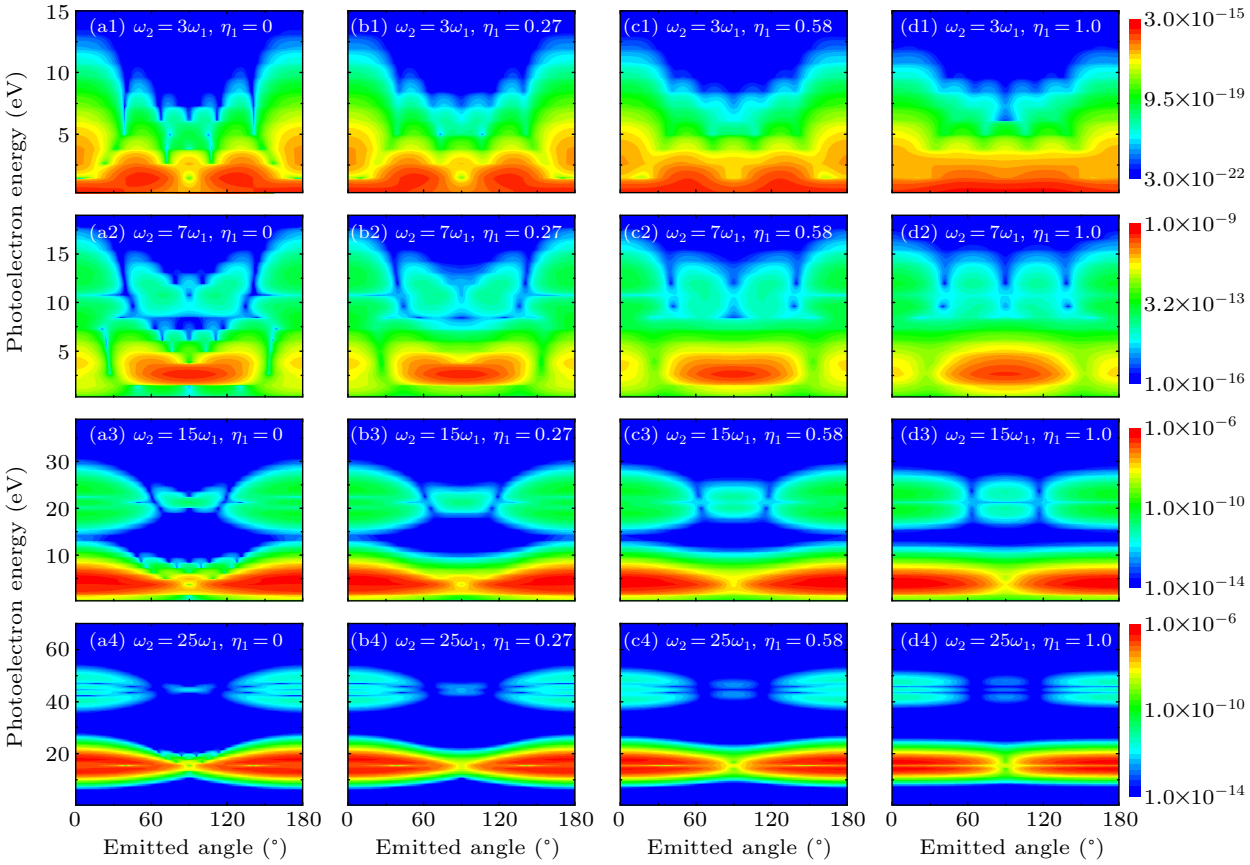


Fig. 2. The angular-resolved ATI spectra for $\omega_2=3\omega_1$ ((a1)–(d1)), $7\omega_1$ ((a2)–(d2)), $15\omega_1$ ((a3)–(d3)) and $25\omega_1$ ((a4)–(d4)). Here panels (a1)–(a4), (b1)–(b4), (c1)–(c4) and (d1)–(d4) correspond separately to $\eta_1=0$, 0.27, 0.58 and 1.0, as well as $\eta_2=0$. The emitted angle is defined as the angle between the x axis and the emission direction of the ionized electron. In logarithmic scale.

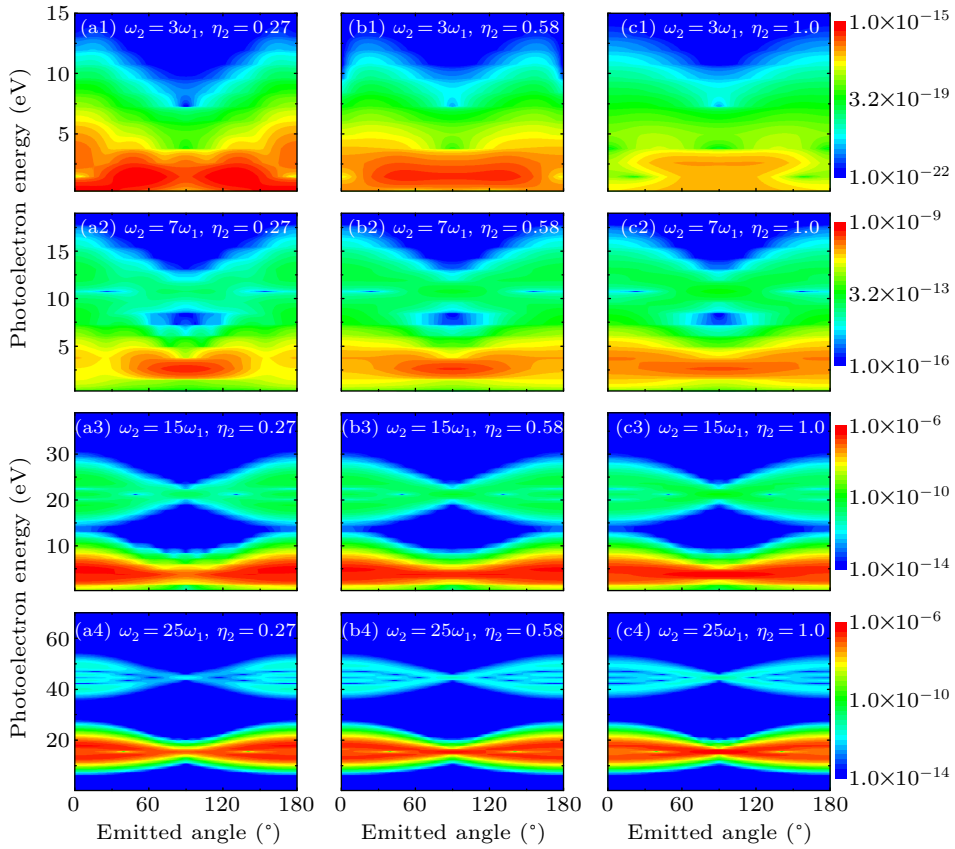


Fig. 3. The angular-resolved ATI spectra for $\omega_2=3\omega_1$ ((a1)–(c1)), $7\omega_1$ ((a2)–(c2)), $15\omega_1$ ((a3)–(c3)), $25\omega_1$ ((a4)–(c4)) and for $\eta_2=0.27$ ((a1)–(a4)), 0.58 ((b1)–(b4)), 1.0 ((c1)–(c4)). Here $\eta_1=0$, and the other parameters are same as that in Fig. 2. In logarithmic scale.

ionization probabilities obviously decrease with the increase of η_2, especially for the emitted angle along the x axis. For $\omega_2 = 7\omega_1$, it is found that the distributions of the lower-energy parts become gradually continuous with the increase of η_2, and the dip structure disappears in Figs. 3(b2) and 3(c2); while there are no evident differences for the distributions of the higher-energy parts with change of the emitted angle, where the energy width for $\varphi_f = 0^\circ$ or 180° is the largest and the energy width for $\varphi_f = 90^\circ$ is the narrowest. For $\omega_2 = 15\omega_1$ and $\omega_2 = 25\omega_1$, the distributions of each plateau are nearly identical for any η_2. It is noticed that there are no dip structures in the angular-resolved ATI spectra, as shown in Figs. 3(a3)–3(c3) and 3(a4)–3(c4), which is different from results shown in Fig. 2. Therefore, it is included that when ω_2 is much more than the ionization potential, the ATI spectrum is independent on the ellipticity η_2 of the high-frequency laser and only depends on the emitted angle φ_f, and dip structure disappears; otherwise the ATI spectrum is determined by η_2 and φ_f.

To uncover the multiplateau formation of the ATI spectrum, the channel may be defined by s_2, which represents the number of photons absorbed by electron from the high-frequency laser. Figure 4 shows the ATI spectrum of different channels. In Fig. 4(a), one can see that the ATI spectra are attributed to the quantum interference between many channels, where channels $s_2 = 3$, 4 and 5 make major contributions to the ATI process. From Figs. 4(b) to 4(d), it is found that the contributions from different channels to the ATI process can be separated gradually with the increase of ω_2, and the interference of these channels decreases. Thus the ATI spectrum shows the multiplateau structure, and the difference of height between neighbouring plateau increases with ω_2. Further, by comparing Fig. 4 with Fig. 2 or Fig. 3, it can be seen that each plateau in the angular-resolved ATI spectrum is from the contribution of certain channels when ω_2 is higher. For example, the first and second plateaus in Figs. 2(a2)–2(d2) or Figs. 3(a2)–3(c2) correspond to the contributions of channels $s_2 = 2$ and $s_2 = 3$ that electron absorbs two and three photons from the high-frequency laser, respectively. When $\omega_2 \geq 15\omega_1$, the first and second plateaus in angular-resolved ATI spectra come separately from the contributions of the channels $s_2 = 1$ and $s_2 = 2$.

Figure 5 shows the angular distributions of different channels for $\omega_2 = 3\omega_1$ under the conditions of different laser ellipticities. For $\eta_1 = \eta_2 = 0$, the ionization probability around the emitted angle $\varphi_f = 60^\circ$ or 120° is mainly from the contribution from the channel $s_2 = 4$, and the higher-energy photoelectron, especially for that along the x axis, is due to the channel $s_2 = 5$. Further, it is clearly seen that with the increase of η_1, the ionization probability of channel $s_2 = 4$ along the y axis is enhanced, while there are little changes in the higher-energy distributions for channel $s_2 = 5$, as illustrated in Figs. 5(b1) and 5(c1), respectively. These results may be in favor to understand the photoelectron distributions shown in Figs. 2(a1)–2(d1). On the other hand, from Figs. 5(a2)–5(c2), one can see that the ionization probability dramatically decreases and the angular distribution also changes obviously with the increase of η_2 for these three channels, which are different from the result shown in Figs. 5(a1)–5(c1).

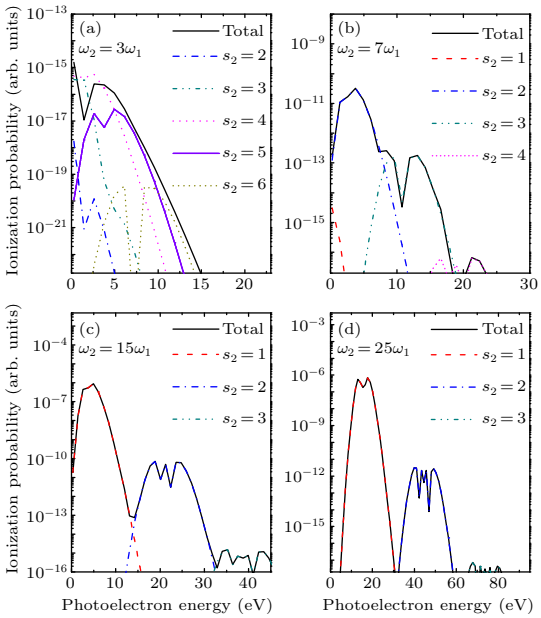


Fig. 4. The ATI spectra of different channels for $\omega_2 = 3\omega_1$ (a), $7\omega_1$ (b), $15\omega_1$ (c), and $25\omega_1$ (d), where s_2 represents the photons absorbed by electron from the high-frequency laser, and the emitted angle is along the x axis, and $\eta_1 = 0.27$, $\eta_2 = 0$.

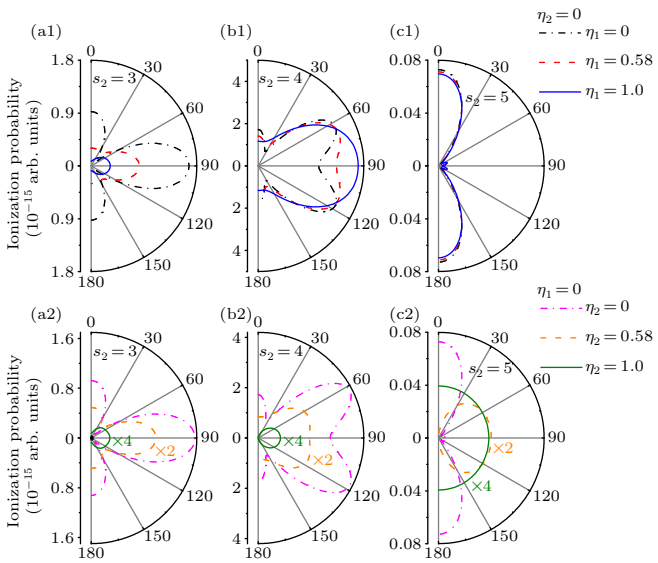


Fig. 5. The angular distributions of channels $s_2 = 3$ ((a1) and (a2)), $s_2 = 4$ ((b1) and (b2)) and $s_2 = 5$ ((c1) and (c2)) for $\omega_2 = 3\omega_1$, where the dash-dotted (black), dashed (red) and solid (blue) lines in the top row separately denote $\eta_1 = 0$, 0.58 and 1.0; the dash-dotted (magenta), dashed (orange) and solid (olive) lines in the bottom row denote $\eta_2 = 0$, 0.58 and 1.0, respectively, and data of $\eta_2 = 0.58$ and 1.0 are separately multiplied by 2 and 4 to put it on scale with $\eta_2 = 0$.

Here Fig. 6 depicts the angular distributions of different channels for $\omega_2 = 7\omega_1$ ((a1)–(d1)) and $\omega_2 = 25\omega_1$ ((a2)–(d2)). One can see that no matter how η_1 is taken in Figs. 6(a1), 6(b1) and 6(a2), 6(b2), the angular distributions have little changes

and keep the same characteristics. By contrast, in Figs. 6(c1), 6(d1) and 6(c2), 6(d2), the angular distributions change significantly with η_2. In Fig. 6(c1), the ionization probability of channel $s_2 = 2$ along the y axis is dominant for $\eta_1 = \eta_2 = 0$, which forms the main lobes, and jet structures appear between the main lobes; the probability along the y axis decreases as the increase of η_2, the probability along the x axis increases, and the jet structure disappears, which may give rise to the isotropic characteristics for $\eta_2 = 1.0$. In Fig. 6(d1), the probability distribution of channel $s_2 = 3$ is opposite to that of channel $s_2 = 2$. The formations of main lobes and jet structures are related to the absorbing photons from the high-frequency laser.[45] For $\omega_2 = 25\omega_1$, the angular distributions of channel $s_2 = 1$ along the x and y axes separately decrease and increase with the increase of η_2, and show the isotropic characteristic for $\eta_2 = 1.0$, which is the same as that of channel $s_2 = 2$. Particularly for both linearly polarized lasers, the angular distributions of the two channels show the main peaks along the x axis. This result is consistent with the one-photon and two-photon ionizations in both recent experiments[34,51] and calculation of solving the full dimensional time-dependent Schrödinger equation.[52]

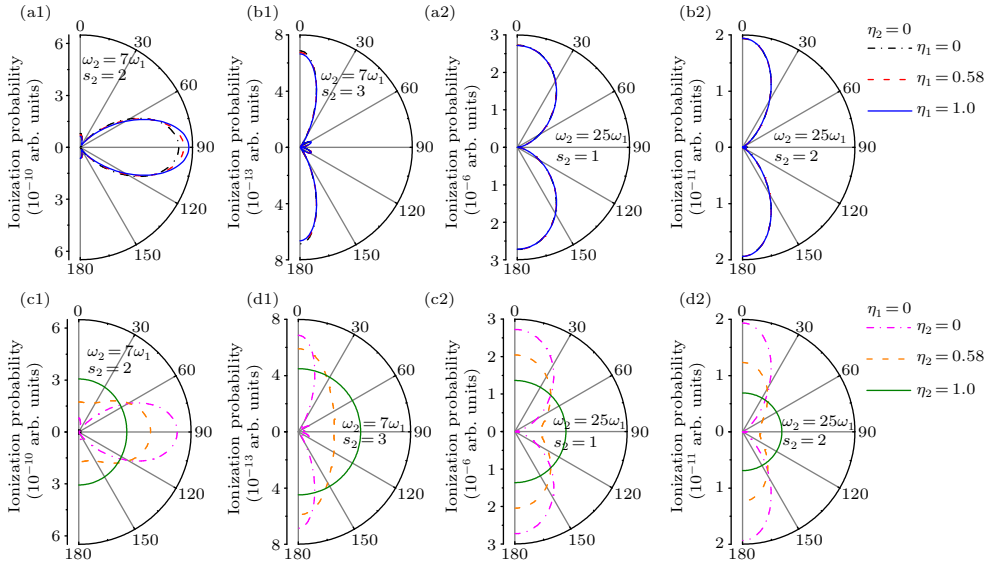


Fig. 6. The angular distributions of different channels for $\omega_2 = 7\omega_1$ ((a1)–(d1)) and $25\omega_1$ ((a2)–(d2)), where the dash-dotted (black), dashed (red) and solid (blue) lines in the top row denote $\eta_1 = 0$, 0.58 and 1.0, respectively; the dash-dotted (magenta), dashed (orange) and solid (olive) lines in the bottom row denote $\eta_2 = 0$, 0.58 and 1.0, respectively.

3.2. Saddle-point approximation and energy orbit

Despite the angular-resolved ATI spectrum shows the complex interference information of atom absorbing photons from the different channels, the spectrum characteristic is determined by the generalized phased Bessel function $\mathcal{X}_{j_1 j_2}(z_f)$ in Eq. (3). In the present laser parameters, the coupling effect between two lasers can be ignored, thus the generalized phased Bessel function $\mathcal{X}_{j_1 j_2}(z_f)$ can be approximated by the phased Bessel function $\mathcal{X}_{j_1 j_2}(z_f) \approx X_{-s_1}(z_1, z_3) X_{-s_2}(z_2, z_4)$, where $X_{-s_1}(z_1, z_3) = \sum_{j_3} X_{-s_1+2j_3}(z_1) X_{-j_3}(z_3)$ and $X_{-s_2}(z_2, z_4) = \sum_{j_4} X_{-s_2+2j_4}(z_2) X_{-j_4}(z_4)$. Here it is easily found that the phased Bessel functions $X_{-s_1}(z_1, z_3)$ and $X_{-s_2}(z_2, z_4)$ are separately related to the IR and high-frequency lasers. Thus the features of ATI spectrum based on $X_{-s_1}(z_1, z_3)$ may be controlled by IR laser, and the information based on $X_{-s_2}(z_2, z_4)$ is determined by XUV laser. Especially, when ω_2 is much more than ω_1, the spectral characteristic may be caused by $X_{-s_1}(z_1, z_3)$ with a weight given by $X_{-s_2}(z_2, z_4)$.[45]

In the following, we will discuss the effect of an elliptically polarized IR laser on the spectrum with the help of the strong-field approximation.[53] Here the IR laser can be viewed as the classical field, and the vector potential can be defined as $\boldsymbol{A}_1(\omega_1 t) = \hat{x} E_{10}/(\omega_1 \sqrt{1+\eta_1^2}) \cos(\omega_1 t) - \hat{y} E_{10} \eta_1/(\omega_1 \sqrt{1+\eta_1^2}) \sin(\omega_1 t)$, where E_{10} is the electric field strength, $\hat{x}$ and $\hat{y}$ are the unit polarization vectors in the x and y directions. In order to analyze the phased Bessel function $X_{-s_1}(z_1, z_3)$ for a certain channel, the explicit integral representation of two-variable phased Bessel function in the following appendix can be written as

$$X_{-s_1}(z_1, z_3) = \frac{1}{T_1} \int_{-T_1}^{T_1} \mathrm{d}t \exp\Big\{ \mathrm{i}|z_1| \sin[\omega_1 t + \arg(z_1)] + \mathrm{i}|z_3| \sin[2\omega_1 t + \arg(z_3)] + \mathrm{i} s_1 \omega_1 t \Big\}, \quad (6)$$

with $T_1 = 2\pi/\omega_1$. On the other hand, the classical action of an electron in an elliptically polarized IR laser field is

$$\begin{aligned} S_{\mathrm{cl}}(\boldsymbol{p}_f, t) &= \int_0^t \frac{(\boldsymbol{p}_f + \boldsymbol{A}_1)^2}{2} \mathrm{d}t \\ &= \frac{p^2}{2} t + U_{p_1} t + |z_1| \sin[\omega_1 t + \arg(z_1)] \\ &\quad + |z_3| \sin(2\omega_1 t). \end{aligned} \quad (7)$$

Comparing Eq. (6) with Eq. (7), and using the energy conservation of the initial and final states during the transition process, the phased Bessel function Eq. (6) can be rewritten as

$$X_{-s_1}(z_1,z_3)=\frac{1}{T_1}\int_{-T_1}^{T_1}\mathrm{d}t\exp\left\{\mathrm{i}\left[S_{\mathrm{cl}}(\boldsymbol{p}_{\mathrm{f}},t)-\left(s_2\omega_2-I_{\mathrm{p}}\right)t\right]\right\}. \tag{8}$$

By applying the saddle-point approximation,[53] the function $X_{-s_1}(z_1,z_3)$ can be approximated by $X_{-s_1}(z_1,z_3)=4\sqrt{\pi}/\left[T_1\sqrt{f''(t_0)}\right]\cos\left[f(t)-\pi/4\right]$. Here t_0 is a saddle point satisfying $f'_{\theta=\omega_1 t_0}(\theta)=0$, which gives rise to the energy conservation relationship

$$\frac{\left[\boldsymbol{p}_{\mathrm{f}}+\boldsymbol{A}_1(\theta)\right]^2}{2}=s_2\omega_2-I_{\mathrm{p}}. \tag{9}$$

Thus the momentum of the ionized electron is obtained as follows:

$$\begin{aligned}\boldsymbol{p}_{\mathrm{f}}(\varphi_{\mathrm{f}},\theta)\ =\ &\sqrt{2(s_2\omega_2-I_{\mathrm{p}})-A_1^2\left(\cos\theta\sin\varphi_{\mathrm{f}}+\eta_1\sin\theta\cos\varphi_{\mathrm{f}}\right)^2}\\&-A_1\left(\cos\varphi_{\mathrm{f}}\cos\theta-\eta_1\sin\varphi_{\mathrm{f}}\sin\theta\right),\end{aligned} \tag{10}$$

where $A_1=E_{10}/\left(\omega_1\sqrt{1+\eta_1^2}\right)$. Further the final energy orbit of ionized electron can be written as $E_{\mathrm{f}}(\varphi_{\mathrm{f}},\theta)=p_{\mathrm{f}}^2/2$, which indicates that the energy orbit is obviously dependent on the ellipticity η_1 of IR laser and the emitted angles of the ionized electron.

Figure 7 shows the channel contributions and corresponding energy orbits for $\omega_2=7\omega_1$ and $\omega_2=25\omega_1$. By comparing Figs. 7(a1), 7(b1) and 7(c1), 7(d1) with Fig. 2(c2) and Fig. 3(b2), it is further verified that the lower- and higher-energy parts for $\omega_2=7\omega_1$ are attributed to the contributions of atom absorbing two and three photons from the high-frequency laser, respectively. The first and second plateaus in the angular-resolved ATI spectra for $\omega_2=25\omega_1$ also correspond to the processes that electron absorbs one and two photons from the high-frequency laser. The maximal and minimal energy orbits predicted by Eq. (10) are illustrated by the solid and dash lines in Fig. 7. One can find that the quantum numerical results are in good agreement with the energy orbits for both $\omega_2=7\omega_1$ and $\omega_2=25\omega_1$. It indicates that the angular-resolved spectrum can be explained by the classical picture: when ω_2 is more than the ionization potential, the electron by absorbing s_2 photons from the high-frequency laser is ionized, then is accelerated or decelerated in the polarized plane by IR laser. Thus the energy width of ATI spectrum can be controlled by the elliptically polarized IR laser, and the height of ATI is determined by the high-frequency laser. This result indicates that the width of the ATI spectrum depends not only on the η_1 but also on the intensity of IR laser, which had been proved in the experiment of Ref. [54]. As one has seen in Figs. 2(d2)–2(d4), the spectral widths for the x and y axes are almost same in the case of circularly polarized IR laser; the energy width is the widest along the polarization direction for the linearly polarized laser. On the other hand, when ω_2 is less than the ionization potential, both the two lasers gradually make identical contributions to the ATI with the decrease of ω_2, and formation of the spectrum is attributed to the interference from many channels.[46]

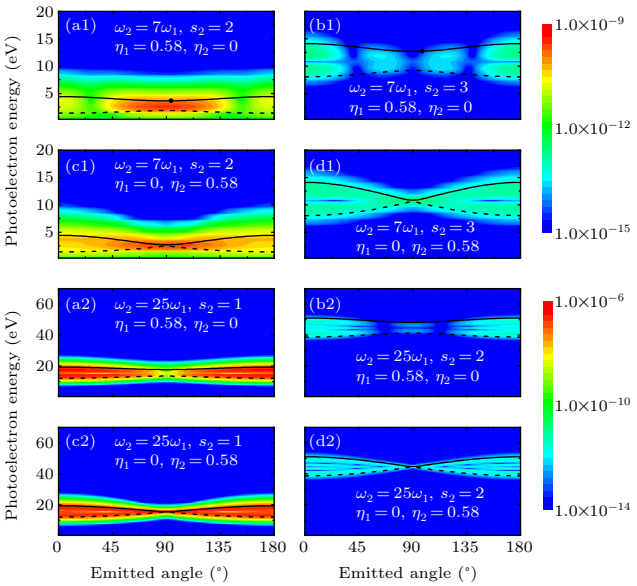


Fig. 7. Channel contributions for $\omega_2=7\omega_1$ ((a1)–(d1)) and $25\omega_1$ ((a2)–(d2)), where ((a1) and (b1)) and ((a2) and (b2)) correspond to $\eta_1=0.58$ and $\eta_2=0$; ((c1) and (d1)) and ((c2) and (d2)) correspond to $\eta_2=0.58$ and $\eta_1=0$. The solid and dashed lines represent the maximal and minimal energies predicted by Eq. (10). In logarithmic scale.

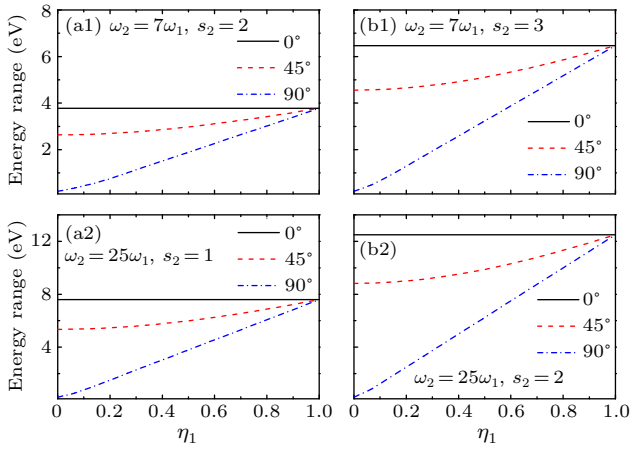


Fig. 8. The channel energy range for $\omega_2=7\omega_1$ ((a1) and (b1)) and $25\omega_1$ ((a2) and (b2)), as function of η_1. The solid (black), dashed (red) and dash-dotted (blue) lines represent the emitted angles 0°, 45° and 90°, respectively.

To reveal the dependence of the elliptically polarized IR laser on the energy width, Fig. 8 shows the energy widths for $\omega_2=7\omega_1$ ((a1) and (b1)) and $\omega_2=25\omega_1$ ((a2) and (b2)). One can see that when the ionized electron is emitted along the angle $\varphi_{\mathrm{f}}=0°$, the energy width is the maximum and does not depend on η_1; the emitted angle $\varphi_{\mathrm{f}}\neq0°$, the energy width increases obviously with η_1. While the more the emitted angle φ_{f} approaches to 90°, the greater the energy width increases.

This result can tell us that the ionized process can be controlled by the ellipticity of the IR laser.

4. Conclusion

We have studied the ATI process of atoms radiated by fundamental and high-frequency lasers with arbitrary ellipticity. It has been seen that the angular-resolved ATI spectra are sensitive to the ellipticities of two lasers, the frequency of the high-frequency laser and emitted angle: (i) when the high-frequency laser is linearly polarized, the energy width of each plateau becomes narrow when emitted angle varies from 0° (180°) to 90° for $\eta_1 \neq 1$, the dip feature in multiplateau structure is shown, and each plateau keeps a certain energy width with the increase of ellipticity of fundamental field; (ii) when the fundamental field is linearly polarized and the frequency of the high-frequency laser is much more than the ionization potential, the ATI spectrum is only determined by the emitted angle, and the dip structure disappears in the case that the high-frequency laser becomes circularly polarized. By the analysis of channel, it is found that the contributions of channels to the ATI spectrum can be separated gradually with the increase of the frequency of the high-frequency laser, and the interference of these channels decreases. Furthermore, when the frequency of high-frequency laser is much lower than ionization potential, the angular distribution depends on the ellipticities of two lasers; otherwise, the angular distribution depends mainly on the ellipticity of high-frequency laser. Moreover, with the help of the saddle-point approximation, the energy conservation relationship in the elliptically polarized IR+XUV two-color laser is obtained, which well predicts the range of each plateau and shows the intuitive picture. Finally, the dependence of the width of each plateau on ellipticity of IR laser is revealed. This work will provide an effective way to polarization control of ATI process in elliptically polarized two-color lasers for experimental research, especially for elliptically polarized IR+XUV two-color fields.

Appendix A: Integral representation of the two-variable phased Bessel function

According to the generating function of ordinary Bessel function $J_n(x)$, the fundamental property $\mathrm{e}^{\mathrm{i}x\sin\theta} = \sum_{n=-\infty}^{\infty} J_n(x)\,\mathrm{e}^{\mathrm{i}n\theta}$ [55] can be expanded as

$$\exp[\mathrm{i}x\sin(\theta+\phi)] = \sum_{n=-\infty}^{\infty} [J_n(x)\exp(\mathrm{i}n\phi)]\exp(\mathrm{i}n\theta). \quad \text{(A1)}$$

Here $X_n(z) \equiv X_n(x,\phi) = J_n(x)\,\mathrm{e}^{\mathrm{i}n\phi}$ with $z = x\mathrm{e}^{\mathrm{i}\phi}$, which is called by the phased Bessel function,[50] and Eq. (A1) can be rewritten as

$$\exp[\mathrm{i}x\sin(\theta+\phi)] = \sum_{n=-\infty}^{\infty} X_n(x,\phi)\exp(\mathrm{i}n\theta). \quad \text{(A2)}$$

Thus

$$\exp[\mathrm{i}x_1\sin(\theta+\phi_1)] = \sum_{n=-\infty}^{\infty} X_n(x_1,\phi_1)\exp(\mathrm{i}n\theta), \quad \text{(A3)}$$

$$\exp[\mathrm{i}x_3\sin(2\theta+\phi_3)] = \sum_{m=-\infty}^{\infty} X_m(x_3,\phi_3)\exp(2\mathrm{i}m\theta). \quad \text{(A4)}$$

By multiplying Eqs. (A3) and (A4), it can be obtained as

$$\begin{aligned}
&\exp[\mathrm{i}x_1\sin(\theta+\phi_1)]\exp[\mathrm{i}x_3\sin(2\theta+\phi_3)] \\
&= \sum_{n=-\infty}^{\infty} X_n(x_1,\phi_1)\exp(\mathrm{i}n\theta)\sum_{m=-\infty}^{\infty} X_m(x_3,\phi_3)\exp(2\mathrm{i}m\theta) \\
&= \sum_{n=-\infty}^{\infty}\sum_{m=-\infty}^{\infty} X_n(x_1,\phi_1)X_m(x_3,\phi_3)\exp[\mathrm{i}(n+2m)\theta]. \quad \text{(A5)}
\end{aligned}$$

Setting $j = n+2m$, Eq. (A5) is expressed by

$$\begin{aligned}
&\exp[\mathrm{i}x_1\sin(\theta+\phi_1)]\exp[\mathrm{i}x_3\sin(2\theta+\phi_3)] \\
&= \sum_{j=-\infty}^{\infty} X_j(z_1,z_3)\exp(\mathrm{i}j\theta), \quad \text{(A6)}
\end{aligned}$$

where

$$X_j(z_1,z_3) = \sum_{m=-\infty}^{\infty} X_{j-2m}(x_1,\phi_1)X_m(x_3,\phi_3), \quad \text{(A7)}$$

which is a two-variable phased Bessel function.[50] Next multiplying both sides of Eq. (A6) by $\mathrm{e}^{-\mathrm{i}m\theta}$ and then integrating the sides, it can be written as

$$\begin{aligned}
&\frac{1}{2\pi}\int_{-\pi}^{\pi}\mathrm{d}\theta\exp(-\mathrm{i}m\theta)\exp[\mathrm{i}x_1\sin(\theta+\phi_1)] \\
&\times\exp[\mathrm{i}x_3\sin(2\theta+\phi_3)] \\
&= \frac{1}{2\pi}\int_{-\pi}^{\pi}\mathrm{d}\theta\sum_{j=-\infty}^{\infty} X_j(z_1,z_3)\exp[\mathrm{i}(j-m)\theta] \\
&= \sum_{j=-\infty}^{\infty} X_j(z_1,z_3)\frac{1}{2\pi}\int_{-\pi}^{\pi}\mathrm{d}\theta\exp[\mathrm{i}(j-m)\theta] \\
&= X_m(z_1,z_3). \quad \text{(A8)}
\end{aligned}$$

Finally the integral representation of the two-variable phased Bessel function is obtained as

$$\begin{aligned}
X_m(z_1,z_3) = \frac{1}{2\pi}\int_{-\pi}^{\pi}\mathrm{d}\theta\exp\big[&\mathrm{i}x_1\sin(\theta+\phi_1) \\
&+\mathrm{i}x_3\sin(2\theta+\phi_3)-\mathrm{i}m\theta\big]. \quad \text{(A9)}
\end{aligned}$$

Acknowledgments

Project supported by the National Natural Science Foundation of China (Grant Nos. 12104285, 12074240, 12204135, 12374260, 12264013, 12204136, 92250303, and 12074418), the Guangdong Basicand Applied Basic Research Foundation (Grant No. 2022A1515011742), the Special Scientific Research Program supported by the Shaanxi Education Department (Grant No. 22JK0423), the Natural Science Basic Research Program of Shaanxi Province of China (Grant Nos. 2023-JC-QN-0085 and 2023-JC-QN-0267), the Hainan Provincial Natural Science Foundation of China (Grant

Nos. 122CXTD504, 123MS002, 123QN179, 123QN180, and 122QN217), the Sino-German Mobility Programme (Grant No. M-0031), the Xi'an Aeronautical Institute 2023 Innovation and Entrepreneurship Training Program for college students (Grant No. S202311736036) and the Course Ideological and Political Education Program (Grant No. 23ZLGC5030).

References

[1] Becker W, Grasbon F, Kopold R, Milošević D B, Paulus G G and Walther H 2002 *Adv. At. Mol. Opt. Phys.* **48** 35
[2] Krausz F and Ivanov M 2009 *Rev. Mod. Phys.* **81** 163
[3] Agostini P, Fabre F, Mainfray G, Petite G and Rahman N K 1979 *Phys. Rev. Lett.* **42** 1127
[4] Tong J, Liu X, Dong W, Jiang W, Zhu M, Xu Y, Zuo Z, Lu P, Gong X, Song X, Yang W and Wu J 2022 *Phys. Rev. Lett.* **129** 173201
[5] Song X, Shi G, Zhang G, Xu J, Lin C, Chen J and Yang W 2018 *Phys. Rev. Lett.* **121** 103201
[6] Liu X, Zhang G, Li J, Shi G, Zhou M, Huang B, Tang Y, Song X and Yang W 2020 *Phys. Rev. Lett.* **124** 113202
[7] Della Picca R, Gramajo A A, Garibotti C R, López S D and Arbó D G 2016 *Phys. Rev. A* **93** 023419
[8] Song X, Xu J, Lin C, Sheng Z, Liu P, Yu X, Zhang H, Yang W, Hu S, Chen J, Xu S, Chen Y, Quan W and Liu X 2017 *Phys. Rev. A* **95** 033426
[9] Ge P, Dou Y, Han M, Fang Y, Guo Z, Wu C, Gong Q and Liu Y 2022 *Phys. Rev. A* **106** 053102
[10] Bai Y, Hao X, Li W, Yang W and Chen J 2023 *Phys. Rev. A* **108** 013115
[11] Cao C, Li M, Liang J, Yan J, Guo K, Li Z, Liu Y, Zhou Y and Lu P 2022 *Phys. Rev. A* **106** 033112
[12] Gong X, Lin C, He F, Song Q, Lin K, Ji Q Y, Zhang W, Ma J, Lu P, Liu Y, Zeng H, Yang W and Wu J 2017 *Phys. Rev. Lett.* **118** 143203
[13] Kerbstadt S, Pengel D, Englert L, Bayer T and Wollenhaupt M 2017 *Phys. Rev. A* **97** 063402
[14] Jin F, Yang W, Liu X, Zhang H, Dong W, Song X and Chen J 2022 *Phys. Rev. Res.* **4** 013140
[15] Zhang L, Xie X, Roither S, Kartashov D, Wang Y, Wang C, Schöffler M, Shafir D, Corkum P B, Baltuška A, Ivanov I, Kheifets A, Liu X, Staudte A and Kitzler M 2014 *Phys. Rev. A* **96** 061401
[16] Habibović D, Gazibegović-Busuladžević A, Busuladžić M and Milošević D B 2021 *Phys. Rev. A* **103** 053101
[17] Wells E, Ben-Itzhak I and Jones R R 2004 *Phys. Rev. Lett.* **93** 023001
[18] Zhao L, Dong J, Lv H, Yang T, Lian Y, Jin M, Xu H and Ding D 2016 *Phys. Rev. A* **94** 053403
[19] Busuladžić M, Gazibegović-Busuladžić A and Milošević D B 2017 *Phys. Rev. A* **95** 033411
[20] Hasović E, Becker W and MiloševićD B 2016 *Opt. Express* **24** 6413
[21] Sviridov A V, Frolov M V, Popruzhenko S V, Geng L and Peng L Y 2022 *Phys. Rev. A* **106** 033117
[22] Čerkić A, Busuladžić M and Miloševic D B 2017 *Phys. Rev. A* **95** 063401
[23] Zhang G P, Si M S, Murakami M, Bai Y H and George T F 2018 *Nat. Commun.* **9** 4727
[24] Huo X X, Xing Y H, Qi T, Sun Y, Li B, Zhang J and Liu X S 2021 *Phys. Rev. A* **103** 053116
[25] Peng L Y, Jiang W C, Geng J W, Xiong W H and Gong Q 2015 *Phys. Rep.* **575** 1
[26] Hofbrucker J, Volotka A V and Fritzsche S 2018 *Phys. Rev. Lett.* **121** 053401
[27] Hofbrucker J, Böning B, Volotka A V and Fritzsche S 2021 *Phys. Rev. A* **104** 013102
[28] Zhai C, Zhu X, Long J, Shao R, Zhang Y, He L, Tang Q, Li Y, Lan P, Yu B and Lu P 2021 *Phys. Rev. A* **103** 033114
[29] Allaria E, Diviacco B, Callegari C, *et al.* 2014 *Phys. Rev. X* **4** 041040
[30] Meyer M, Cubaynes D, Glijer D, Dardis J, Hayden P, Hough P, Richardson V, Kennedy E T, Costello J T, Radcliffe P, Düsterer S, Azima A, Li W B, Redlin H, Feldhaus J, Taïeb R, Maquet A, Grum-Grzhimailo A N, Gryzlova E V and Strakhova S I 2014 *Phys. Rev. X* **4** 041040
[31] Zhao X, Wei H, Yu W W and Lin C D 2018 *Phys. Rev. A* **98** 053404
[32] Lin C D, Le A T, Chen Z, Morishita T and Lucchese R 2010 *J. Phys. B* **43** 122001
[33] Düsterer S, Rading L, Johnsson P, Rouzée A, Hundertmark A, Vrakking M J J, Radcliffe P, Meyer M, Kazansky A K and Kabachnik N M 2013 *J. Phys. B* **46** 164026
[34] Düsterer S, Hartmann G, Babies F, Beckmann A, Brenner G, Buck J, Costello J, Dammann L, De Fanis A, Geßler P, Glaser L, Ilchen M, Johnsson P, Kazansky A K, Kelly T J, Mazza T, Meyer M, Nosik V L, Sazhina I P, Scholz F, Seltmann J, Sotoudi H, Viefhaus J and Kabachnik N M 2016 *J. Phys. B* **49** 165003
[35] Guo D S and Drake G W F 1992 *J. Phys. A: Math. Gen.* **25** 5377
[36] Guo D S, Åberg T and Crasemann B 1989 *Phys. Rev. A* **40** 4997
[37] Cheng T, Li X, Ao S, Wu L and Fu P 2003 *Phys. Rev. A* **68** 033411
[38] Gao L, Li X, Fu P, Freeman R R and Guo D S 2000 *Phys. Rev. A* **61** 063407
[39] Wang B, Gao L, Li X, Guo D S and Fu P 2007 *Phys. Rev. A* **75** 063419
[40] Wang B, Guo Y, Chen J, Yan Z C and Fu P 2012 *Phys. Rev. A* **85** 023402
[41] Jin F, Chen J, Yang Y, Liu X, Yan Z C and Wang B 2018 *J. Phys. B* **51** 035601
[42] Jin F, Tian Y, Chen J, Yang Y, Liu X, Yan Z C and Wang B 2016 *Phys. Rev. A* **93** 043417
[43] Fu P, Wang B, Li X and Gao L 2001 *Phys. Rev. A* **64** 063401
[44] Jin F, Yang H, Wang B, Wei L and Wu H 2019 *Opt. Express* **27** 20754
[45] Jin F, Yang H, Zhang H, Wang B and Yang W 2021 *Opt. Express* **29** 10726
[46] Liu M, Guo Y and Wang B 2015 *Chin. Phys. B* **24** 073201
[47] Zhang K, Chen J, Hao X L, Fu P, Yan Z C and Wang B 2013 *Phys. Rev. A* **88** 043435
[48] Reiss H R 1980 *Phys. Rev. A* **22** 1786
[49] Becker A and Faisal F H M 2005 *J. Phys. B* **38** R1
[50] Hu X, Wang H and Guo D S 2008 *Can. J. Phys.* **86** 863
[51] Ma H, Wang X, Zhang L, Zou Z, Yuan J, Ma Y, Lv R, Shen Z, Yan T, Weidemüller M, Ye D and Jiang Y 2023 *Phys. Rev. A* **107** 033114
[52] Boll D I R, Fojón O A, McCurdy C W and Palacios A 2019 *Phys. Rev. A* **99** 023416
[53] Milošević D B and Ehlotzky F 2003 *Adv. At. Mol. Opt. Phys.* **49** 373
[54] Minemoto S, Shimada H, Komatsu K, Komatsubara W, Majima T, Mizuno T, Owada S, Sakai H, Togashi T, Yoshida S, Yabashi M and Yagishita A 2018 *J. Phys. B* **51** 075601
[55] Lötstedt E and Jentschura U D 2009 *Phys. Rev. E* **79** 026707